

The Influence of Viscoelasticity on the Dynamics of Encapsulated Microbubbles Near a Rigid Surface Forced by Ultrasound

M.J.Walters^{1, a)} and T.N.Phillips^{1, b)}

School of Mathematics, Cardiff University, Cardiff CF24 4AG, UK

(Dated: 20 January 2017)

The dynamics of thin-shell encapsulated microbubbles (EMBs) in viscoelastic fluids forced by ultrasound are investigated in this paper. EMBs, which are gas-filled microbubbles encased in a stiff albumin or flexible lipid shell, have been shown to improve the performance of biomedical procedures such as ultrasound contrast imaging and sonoporation. The viscoelastic fluid is modelled using the Oldroyd B model while the properties of the shell are accounted for through the dynamic boundary condition at the bubble surface. The effects of fluid viscoelasticity on the dynamics of an EMB are found to be similar to those found for a clean cavitation bubble. Fluid viscosity tends to have an inhibitive effect on fluid jet velocities although the dynamics are governed by a competition between viscous, elastic and inertial forces. A larger response is observed for lower frequency ultrasound although for pressure amplitudes typical to sonoporation, large translational movement in the direction of the pulse is predicted as well as the potential for bubble fragmentation.

Keywords: Boundary element method, encapsulated bubbles, viscoelasticity, ultrasound

I. INTRODUCTION

Ultrasound is one of the predominant methods for medical diagnosis since it is safe, fast and inexpensive compared to other techniques. While the image quality using conventional procedures is often unsatisfactory, it can be significantly improved through the introduction of encapsulated microbubbles (EMBs). The interaction of an ultrasound beam with a microbubble causes the bubble to expand and contract since the internal gas is much more compressible than the surrounding tissue. For a typical EMB of the order $1\mu\text{m}$, this occurs most readily for the resonance frequency lying in the range (2 - 10MHz), which is the range typically used for ultrasound imaging (Cosgrove (2006)). Due to this, EMBs return significantly stronger echoes than tissue reflectors of a similar size and it is this property that is responsible for their efficacy as contrast agents.

An EMB, also known as an ultrasound contrast agent (UCA), is typically filled with air or a high-molecular-weight low-solubility gas encased by an albumin or lipid shell. The bubbles are typically $1 - 10\mu\text{m}$ in diameter (Wells (2006)) which is small enough to pass through capillaries when suspended in blood. The encapsulating shell stabilises the bubble against surface tension effects and consequently an EMB is able to reach almost any desired area of the body without collapsing or dissolving. In recent years, targeted contrast agents have also been developed to selectively adhere to a specific site (Doinikov, Zhao, and Dayton (2009)). Recently, EMBs have also been investigated for use in sonoporation (Bao, Thrall, and Miller (1997)) and gene therapy (Miller, Pislaru, and Greenleaf (2002)). Sonoporation is the use of ultrasound to increase the permeability of cell membranes; ideally

creating transient pores which allow the uptake of large molecules such as DNA into a cell without destroying it (known as transfection). The molecules can be transferred to the desired site using EMBs, which are then excited using an ultrasound field. The physics behind the increased cell permeability and the transfection of the material are complex, although Miller, Pislaru, and Greenleaf (2002) have been shown that cavitation bubbles play a role.

The majority of previous numerical studies on EMBs have investigated spherical oscillations, usually involving a modified Rayleigh-Plesset equation with extra terms accounting for the properties of the shell (see, for example, Church (1995) and Hoff (2001)). Although the shell has a stabilising effect on the bubble dynamics, non-spherical behaviour of EMBs can still occur due to the presence of nearby structures or interaction with a strong ultrasound field. In a recent paper, Wang, Manmi, and Calvisi (2015) used the boundary element method (BEM) to model a non-spherical EMB near a rigid surface that is forced by ultrasound. A modification of Hoff's spherical model was used and applied through the dynamic boundary condition at the bubble surface. The majority of the results presented were for an inviscid fluid although some Newtonian examples were also considered. However, neither biological fluids nor soft tissue behave as Newtonian fluids. Therefore, the challenge in studying the behaviour of EMBs in a biomedical context lies in modelling viscoelastic and compressible behaviour.

In terms of compressibility, direct numerical simulations have been largely restricted to inviscid and Newtonian fluids (Johnsen and Colonius (2008, 2009)). The simulations of the full governing system of equations that have been performed for viscoelastic fluids have been largely based on Maxwell-type models in which compressibility is neglected (Lind and Phillips (2010), Foteinopoulou and Laso (2010)). However, Lind and Phillips (2013) considered the non-spherical collapse of a

^{a)} Electronic mail: WaltersMJ1@cf.ac.uk

^{b)} Electronic mail: PhillipsTN@cf.ac.uk

bubble near a rigid wall in a weakly compressible upper-convected Maxwell fluid and showed that viscoelasticity can prevent the formation of a liquid jet and is therefore likely to mitigate cavitation damage.

A primary characteristic of spherical bubble collapse (or expansion) in most viscoelastic fluids, is the oscillation of the bubble radius in time. This effect is essentially due the competition between inertial and elastic forces and occurs only in fluids with characteristically large elasticities, such as the Maxwell and Oldroyd models (it is consequently not seen in a second order fluid). Many authors have noted this and other effects by solving a generalised Rayleigh-Plesset equation for a range of different constitutive relations. Fogler and Goddard (1970) undertook one of the first theoretical studies of collapse in a viscoelastic medium using a Rayleigh-Plesset equation to solve the problem of a collapsing spherical cavity in a linear Maxwell fluid. For a range of Reynolds and Deborah numbers, the viscoelastic Rayleigh-Plesset equation was solved using finite difference methods. Their results showed that for very large Deborah numbers the bubble will either oscillate about an equilibrium radius, or collapse without oscillation, depending on some critical value. The most important finding of the study was that fluid elasticity can significantly retard the collapse of a void and produce large oscillatory motion whenever the relaxation time of the fluid is of the same order of magnitude as the Rayleigh collapse time.

Allen and Roy (2000a,b) considered the forced oscillation of a bubble in a infinite expanse of fluid using incompressible linear and nonlinear Maxwell models. They found significant differences between Newtonian and viscoelastic cases. In particular, Allen and Roy (2000a) showed that there were significant differences between the viscoelastic and Newtonian cases with the addition of elasticity when studying subharmonic oscillations modulates the amplitude corresponding to the relaxation time of the fluid. Allen and Roy (2000b) extended the analysis to study the oscillation of bubbles in nonlinear viscoelastic media. Agreement with the predictions of linear viscoelasticity was found for small deformations. However, it was also found that beyond the limit of small deformations, elasticity can increase the generation of secondary harmonics and serve to increase the maximum bubble radius. Since cavitation damage has been linked to large bubble expansions this is an important discovery in the context of bubble dynamics in biological fluids and tissue.

Khismatullin and Nadim (2002) performed a theoretical investigation of the small-amplitude oscillations of a microbubble encapsulated by a viscoelastic shell and immersed in a slightly compressible viscoelastic fluid. The viscoelastic properties of the shell and the liquid were modelled using the Kelvin-Voigt and 4-constant Oldroyd models, respectively. The method of matched asymptotic expansions is used to derive an equation for the radial oscillation of the bubble. They showed that the resonance frequency for the EMB is highly dependent on viscous damping and therefore, significantly differs from

the undamped natural frequency. The effects of the shell and liquid parameters on the resonance frequency and scattering cross sections are analyzed.

Yang and Church (2005) investigated the large-amplitude oscillations of cavitation bubbles driven by an ultrasonic field using the Keller-Miksis equation in conjunction with a Kelvin-Voigt model to describe viscoelasticity. They found that elasticity increases the inertial cavitation threshold, and subharmonic signals may only be detectable in certain ranges of radius and pressure amplitude.

Brujan (1999, 2009) investigated spherical bubble dynamics in a compressible viscoelastic liquid using a linear Oldroyd model and a simplified singular-perturbation method to first-order in the bubble-wall Mach number. He showed that, under conditions comparable to those existing during cavitation, the effect of fluid rheology on bubble dynamics is negligible for values of the Reynolds number beyond a critical value while the only significant influence is that of liquid compressibility. For larger values of the Reynolds number sound emission was found to be the main damping mechanism. In both cases, the $1/r$ law of pressure attenuation through the liquid was not affected by the viscoelastic properties of the liquid.

Brujan (2009) noted that in order to gain a full understanding of the behaviour of cavitation bubbles in non-Newtonian liquids, it is necessary to extend theoretical studies to the case of asymmetric collapse of bubbles since some experiments have indicated that the effect of fluid viscoelasticity is more evident in bubbles collapsing in the neighbourhood of a solid boundary, altering the intensity of the liquid jet directed toward to boundary.

The present study follows a similar approach to the one employed by Wang, Manmi, and Calvisi (2015) and seeks to extend previous studies on modelling EMBs forced by ultrasound by determining the effects of elasticity and shell properties on the bubble dynamics. Viscoelasticity is modelled using the Oldroyd B model which is able to account for both solvent and polymeric behaviour. This model is able to describe a range of viscoelastic behaviour and can be implemented within the boundary element methodology. The numerical approach is used to predict the dynamics of an EMB located near a rigid wall following its excitation by an ultrasound field. The mathematical models for spherical EMBs, based on a modified Rayleigh-Plesset equation, and non-spherical EMBs, using a modified Bernoulli equation, are described in Sec. II. This is followed in Sec. III by a description of a non-singular boundary element method that removes the singularity in the kernel and which can model the transition to toroidal dynamics. Numerical results are presented in Sec. IV in which the effects of shell width, viscoelasticity and ultrasound properties on bubble dynamics are described. Finally, some concluding remarks are made in Sec. V.

II. MATHEMATICAL MODEL

The aim of the present study is to understand how elasticity of the fluid and the shell affects the dynamics of encapsulated microbubbles in a viscoelastic fluid forced by ultrasound. This problem is a modification of the simple Rayleigh collapse problem.

A. Bubble Dynamics for Spherical EMBs

It is well known that the oscillations of a clean, spherical cavitation bubble in an infinite expanse of incompressible fluid can be described by the Rayleigh-Plesset equation. The Rayleigh-Plesset equation was originally derived by Rayleigh (1917) for an empty cavity or void. Recently, a number of modifications to the Rayleigh-Plesset equation have been developed to describe spherical encapsulated bubbles. Assuming the shell is thin and Newtonian, the following modified Rayleigh-Plesset equation can be derived

$$R\ddot{R} + \frac{3}{2}\dot{R}^2 = \frac{1}{\rho} \left[p_B - p_\infty - \tau_{rr}^{(sh)}|_R + \tau_{rr}|_R - 12\eta^{(sh)}\varepsilon \frac{\dot{R}}{R(R-\varepsilon)} - 2 \int_R^\infty \left(\frac{\tau_{rr} - \tau_{\theta\theta}}{r} \right) dr \right], \quad (1)$$

where $R(t)$ is the radius of the bubble, the dot denotes the time derivative, ρ is the density of the surrounding fluid, p_∞ is the (undisturbed) pressure at infinity, τ is the extra stress tensor with superscript (sh) denoting shell quantities, $\eta^{(sh)}$ is the shell viscosity and ε is the shell thickness. The term describing the effect of viscous shell damping in Eqn. (1) is derived by employing the thin shell approximation

$$2 \int_{R_1}^{R_1+\varepsilon} \left(\frac{\tau_{rr}^{(sh)} - \tau_{\theta\theta}^{(sh)}}{r} \right) dr \approx -12\eta^{(sh)}\varepsilon \frac{\dot{R}}{R(R-\varepsilon)}, \quad (2)$$

where higher order terms in ε have been neglected (Morgan *et al.* (2000)). The pressure on the liquid side of the interface is determined by balancing the normal stresses

$$p_B = p_i - \frac{2\sigma}{R} - \tau_{rr} + \tau_{rr}^{(sh)} - \frac{2\chi}{R} \left(\frac{R_0}{R} \right)^2, \quad (3)$$

where σ is the interfacial tension coefficient and κ is the elasticity modulus of the shell. The final term on the right-hand side of (3) is derived by accounting for the changing interfacial tension due to the varying bubble radius (and assuming an instantaneous thermodynamic equilibrium during bubble oscillations). A more detailed derivation of this term can be found in the paper by Glazman (1983). Using the polytropic law then gives

$$p_i \left(\frac{4}{3}\pi R^3 \right)^\kappa = \text{constant}, \quad (4)$$

where κ is the ratio of specific heats for the gas. Thus the internal bubble pressure is

$$p_i = p_{i,eq} \left(\frac{R_0}{R} \right)^{3\kappa}$$

where

$$p_{i,eq} = \left(p_0 + \frac{2\sigma}{R_0} + \frac{2\chi}{R_0} \right). \quad (5)$$

A complete derivation of Eqn. (1) can be found in Walters (2015).

B. Bubble Dynamics for Nonspherical EMBs

Consider an initially spherical bubble whose centroid is a distance h from a horizontal rigid boundary of infinite extent. The bubble is assumed to remain axisymmetric in time since this is generally found to be the case for small cavitation bubbles (Brennen (1995)). Additionally, it is the axisymmetric configuration that generates maximum jet speeds and pressures and thus provides an indication of the maximum potential damage to nearby surfaces.

The fluid is assumed to be incompressible and irrotational. In order to formulate a velocity potential, ϕ , which satisfies Laplace's equation, it is necessary to assume incompressibility. The primary condition needed for this approximation to be valid is

$$M^2 \ll 1, \quad (6)$$

where $M = U/c$ is the Mach number, c is the speed of sound in the liquid and U is the magnitude of variations of the fluid velocity with respect to both position and time (Batchelor (1967)). Brujan (2001) noted that in the late stages of collapse when a jet forms the bubble wall velocities can approach the speed of sound which means that condition (6) is violated and liquid compressibility can no longer be ignored. These high velocities also give rise to very large pressures in the fluid.

It is assumed that the bulk viscosity of the fluid is negligible. The effects of viscosity and fluid rheology are typically only important in thin boundary layers near the bubble surface and thus can be modelled approximately through a boundary condition at the bubble interface (Batchelor (1967); Lind and Phillips (2010)). This approximation has been justified and used in Lind and Phillips (2010) and Walters (2015). Comparisons of predictions using BEM with the direct solution of the Rayleigh-Plesset equation for a spherical bubble have shown that qualitatively similar results are produced but the BEM model predicts slightly larger amplitude oscillations (Walters (2015)).

For a cavitation bubble with a 'clean' surface, the pressure on the fluid side of the bubble interface, p_B is given by

$$p_B = -\rho \frac{D\phi}{Dt} + \frac{\rho}{2} |\nabla \phi|^2 + p_\infty, \quad (7)$$

where D/Dt is the material derivative and ϕ is the velocity potential; defined as $\nabla\phi = \mathbf{u}$ where \mathbf{u} is the velocity field. If we assume there is no mass transfer through the bubble wall and neglect surface tension, then balancing normal forces across the surface results in

$$\begin{aligned}\sigma_{nn}(\text{liquid}) &= -p_B + \tau_{nn} = \sigma_{nn}(\text{gas}) \\ &= -p_i\end{aligned}\quad (8)$$

where p_i is the internal pressure of the bubble, given by

$$p_i(t) = p_0 \left(\frac{R_0}{R} \right)^{3\kappa}, \quad (9)$$

where p_0 is the (initial) internal gas pressure. Combining (7) and (8) to eliminate p_B gives the Bernoulli equation, which is used to update ϕ on the bubble surface

$$\rho \frac{D\phi}{Dt} = \frac{\rho}{2} |\nabla\phi|^2 - \tau_{nn} + \sigma C + p_\infty - p_i, \quad (10)$$

To model an EMB using the boundary element method, a generalisation of the spherical model described in the previous section is developed. In the case of a spherical bubble, the pressure over the bubble surface is constant at each instant in time whereas for a non-spherical bubble the pressure varies locally over the bubble surface. In the boundary element method, the bubble surface is decomposed into a number (N) of segments separated by $N + 1$ nodes. To modify Eqn. (7) for a non-spherical bubble the radius R is replaced by the local radius $R_c(s)$ at each node where s denotes arclength. This can be calculated using $R_c(s) = 1/C(s)$ where $C(s)$ is the local radius of curvature defined by

$$C(s) = -\frac{(r'(s)z''(s) - z'(s)r''(s))}{(r'(s)^2 + z'(s)^2)^{3/2}}, \quad (11)$$

where $r(s)$ and $z(s)$ are the coordinates of nodes on the bubble surface. The derivatives in Eqn. (11) can be determined by constructing quintic spline representations for $r(s)$ and $z(s)$. The pressure at each node is then calculated using

$$p_B = \left(p_{g0} + \frac{2\chi}{R_0} \right) \left(\frac{R_0}{R_c} \right)^{3\kappa} - \tau_{rr} + \tau_{rr}^{(sh)} - \frac{2\chi}{R_c} \left(\frac{R_0}{R_c} \right)^2. \quad (12)$$

Note that this is Eqn. (3) with R replaced by the local quantity $R_c(s)$ at each node. In the same manner as the interfacial term, the radius R is replaced by $R_c(s)$ and the velocity becomes $\partial\phi/\partial n$ in the viscous shell damping term (2). The Bernoulli equation used to update ϕ for a non-spherical EMB is

$$\begin{aligned}\rho \frac{D\phi}{Dt} &= p_\infty - \left(p_0 + \frac{2\chi}{R_0} \right) \left(\frac{V_0}{V} \right)^\kappa + \frac{\rho}{2} |\nabla\phi|^2 - 2\eta^{(sh)} \frac{\partial^2\phi}{\partial n^2} \\ &+ \frac{2\chi}{R_c} \left(\frac{R_0}{R_c} \right)^2 - \frac{12\eta^{(sh)}\varepsilon}{R_c(R_c - \varepsilon)} \frac{\partial\phi}{\partial n} - \tau_{nn}.\end{aligned}\quad (13)$$

The bubble surface must also be updated in time. Since the bubble surface is stress-free, fluid particles which begin on the surface will remain there and thus the surface can be updated in a Lagrangian manner using

$$\frac{D\mathbf{x}}{Dt} = \nabla\phi, \quad (14)$$

where \mathbf{x} is a point on the bubble surface. To integrate Eqns. (13) and (14) in time, a constitutive equation must be chosen for the stress while the normal velocities $\partial\phi/\partial n$ are determined by solving a boundary integral equation.

C. Modelling Viscoelasticity

Finally, a constitutive equation is required to provide a relationship between the stress and strain. One of the aims of this paper is to understand the effects of viscoelasticity on bubble dynamics. Therefore fluid rheology is modelled using the Oldroyd-B model which is chosen since it is sophisticated enough to model a range of rheological behaviour. The model predicts stress relaxation, constant shear viscosity and quadratic first normal stress difference. For the Oldroyd-B model the extra stress $\boldsymbol{\tau}$ can be decomposed in terms of its solvent and polymeric contributions

$$\boldsymbol{\tau} = \boldsymbol{\tau}^s + \boldsymbol{\tau}^p, \quad (15)$$

where

$$\boldsymbol{\tau}^s = 2\eta_s \nabla\mathbf{u}, \quad \boldsymbol{\tau}^p + \lambda \nabla \nabla \boldsymbol{\tau}^p = 2\eta_p \nabla\mathbf{u}. \quad (16)$$

In these equations η_s , η_p and λ are the solvent viscosity, polymeric viscosity and relaxation time of the fluid, respectively. In terms of the normal stress component τ_{nn} the relevant equations for the solvent and polymeric contributions to the stress become

$$\tau_{nn}^s = 2\eta_s \frac{\partial^2\phi}{\partial n^2}, \quad (17)$$

$$\lambda_1 \frac{D\tau_{nn}^p}{Dt} = -\tau_{nn}^p - 2\lambda \tau_{nn}^p \frac{\partial^2\phi}{\partial n^2} - 2\eta_p \frac{\partial^2\phi}{\partial n^2}. \quad (18)$$

III. NON-SINGULAR BEM FORMULATION

In the standard BEM formulation, the potential satisfies the boundary integral equation (see, for example, Taib (1985))

$$c(\mathbf{p})\phi(\mathbf{p}) = \int_{\partial\Omega} \left(\frac{\partial\phi}{\partial n}(\mathbf{q})G(\mathbf{p}, \mathbf{q}) - \phi(\mathbf{q}) \frac{\partial G}{\partial n}(\mathbf{p}, \mathbf{q}) \right) dS, \quad (19)$$

where $c(\mathbf{p})$ is a piecewise constant, Ω and $\partial\Omega$ are the fluid domain and its boundary, respectively, and \mathbf{p}, \mathbf{q} are points in the fluid and on the boundary, respectively. To solve (19) numerically, the bubble surface is discretised

into N segments and (19) is collocated at points $\mathbf{p} = \mathbf{p}_i$, $i = 1, \dots, N + 1$,

$$\begin{aligned} c(\mathbf{p}_i)\phi(\mathbf{p}_i) + \sum_{j=1}^N \int_{s_j}^{s_{j+1}} \phi(\mathbf{q}) \frac{\partial G}{\partial n}(\mathbf{p}_i, \mathbf{q}) dS \\ = \sum_{j=1}^N \int_{s_j}^{s_{j+1}} \frac{\partial \phi}{\partial n}(\mathbf{q}) G(\mathbf{p}_i, \mathbf{q}) dS, \end{aligned} \quad (20)$$

where s_j is the arclength of the bubble surface at node j and the known quantities are on the left-hand side. Given the potential ϕ at each node, Eqn. (20) can be used to solve for the normal velocities $\partial \phi(\mathbf{p}_i)/\partial n$. However, when an integral over a segment in (20) contains the collocation point \mathbf{p}_i , both G and $\partial G/\partial n$ will possess a singularity. Following Sun *et al.* (2014), singularities are removed from the boundary integral equation by defining new variables

$$\psi_i(\mathbf{p}) = \phi(\mathbf{p}_i) + \left(\frac{\partial \phi}{\partial n} \right)_i f_i(\mathbf{p}), \quad (21)$$

for $i = 1, \dots, N + 1$, where the functions f_i are constructed to satisfy

$$\nabla^2 f_i(\mathbf{p}) = 0, \quad f_i(\mathbf{p}_i) = 0, \quad \frac{\partial f_i}{\partial n}(\mathbf{p}_i) = 1. \quad (22)$$

Writing an integral equation for the new variables and subtracting it from (19) a non-singular formulation of the integral equation can be derived (see Walters and Phillips (2016))

$$\begin{aligned} \int_S \left[\phi(\mathbf{q}) - \phi(\mathbf{p}_i) \right] \frac{\partial G}{\partial n}(\mathbf{p}_i, \mathbf{q}) dS = \int_S \frac{\partial \phi}{\partial n} G(\mathbf{p}_i, \mathbf{q}) \\ + \left(\frac{\partial \phi}{\partial n} \right)_i \int_S \left(f_i(\mathbf{q}) \frac{\partial G}{\partial n}(\mathbf{p}_i, \mathbf{q}) - \frac{\partial f_i}{\partial n}(\mathbf{q}) G(\mathbf{p}_i, \mathbf{q}) \right) dS. \end{aligned} \quad (23)$$

The careful construction of the functions f_i , satisfying the properties described by (22) ensures that singularities present in G and $\partial G/\partial n$ are removed.

For a bubble near a rigid wall, the no-penetration condition at the wall results in the following form for the functions f_i , given by

$$f_i(\mathbf{p}) = -\frac{\rho_i^3 \bar{\rho}_i^3}{\bar{\rho}_i^3 \beta_i + \rho_i^3 \bar{\beta}_i} \left[\left(\frac{1}{\rho} - \frac{1}{\rho_i} \right) + \left(\frac{1}{\bar{\rho}} - \frac{1}{\bar{\rho}_i} \right) \right], \quad (24)$$

where

$$\begin{aligned} \rho = \sqrt{r^2 + (z - z_D)^2}, \quad \bar{\rho} = \sqrt{r^2 + (z + z_D)^2}, \\ \beta = rn_r + (z - z_D)n_z, \quad \bar{\beta} = rn_r + (z + z_D)n_z, \end{aligned} \quad (25)$$

and the suffix i indicates evaluation at $(r_i, 0, z_i)$. In this representation $\mathbf{p}_D = (0, 0, z_D)$ is chosen to be any point located outside the domain, provided that $\mathbf{n}_i \cdot (\mathbf{p}_i - \mathbf{p}_D) \neq 0$. The point \mathbf{p}_D is chosen to be located on the z -axis to

ensure that ψ_i defined by (21) are axisymmetric functions. This ensures that the functions f_i are constant in θ and therefore do not appear in the azimuthal integrals contained in (23). Full details of this derivation can be found in Walters and Phillips (2016).

To discretise the bubble surface, quintic splines are chosen. The surface variables, potential and extra stress are represented in each segment (s_i, s_{i+1}) by a fifth order polynomial. Quintic splines have been shown (Walters and Phillips (2016)) to be more accurate and stable than cubic splines. To attain a prescribed level of accuracy far fewer nodes are required when quintic splines are used.

A. Toroidal Bubble

The presence of a rigid wall or the application of an ultrasound field can cause a liquid jet to form during bubble collapse. If the jet is sufficiently strong, it can eventually impact the far side of the bubble wall. When this happens the bubble undergoes a change of topology and becomes toroidal. To model this topological singularity using the BEM formulation described above, the vortex ring method developed by Wang *et al.* (2005) is used. Just prior to jet impact, the bubble surface is smoothed around the impact site and a vortex ring is seeded inside the bubble to account for the jump in velocity potential and the circulation that is present in the post-impact flow. The potential ϕ is decomposed as follows

$$\phi(r, z, t) = \varphi^{vr}(r, z) + \varphi(r, z, t), \quad (26)$$

where φ^{vr} and φ are the vortex potential and remnant potential, respectively. The vortex potential can be found using either the Biot-Savart Law or using solid angle formulae. Once φ^{vr} is found, Eqn. (26) is used to calculate the remnant potential. The remnant potential is smooth in space and time and can be updated using a Bernoulli equation in a similar manner as for the singly-connected bubble described earlier.

The position of the vortex ring within the bubble is unimportant provided it lies completely within the bubble. Thus it remains in a fixed position until the evolving bubble surface requires it to be relocated. More details of the vortex ring method can be found in Walters (2015) and Wang *et al.* (2005).

B. Modelling the Pressure Field

To simulate the interaction between ultrasound and an encapsulated bubble, a Gaussian acoustic pulse is used. The pulse is assumed to be much larger than the bubble and is thus approximated as being infinite in width (infinitely large in the direction perpendicular to the wave propagation). This pulse is incorporated into the model by modifying the pressure term $p_\infty(\mathbf{x}, t)$. The explicit

form for the Gaussian pulse at a fixed point is

$$p_{\infty}(t) = p_0 + p_A \sin[2\pi f(t - t_p)] \exp[-\pi^2 h^2 f^2 (t - t_p)^2], \quad (27)$$

where p_A is the maximum amplitude of the pulse, f is the frequency, t_p is the centre of the pulse and h is the width of the pulse. Fig. 1 shows the pulse as a function of time at a fixed point in space for $f = 2\text{MHz}$ and $p_A = 200\text{kPa}$.

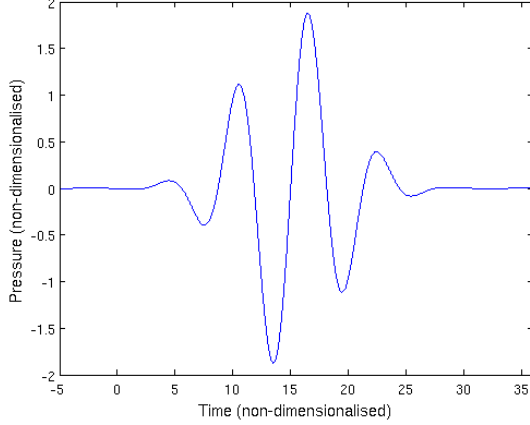


FIG. 1. Typical Gaussian pulse as a function of time with $p_A = 200\text{kPa}$ and $f = 2\text{MHz}$

Since the pulse has a frequency f it is natural to use the following non-dimensionalisation

$$t = \frac{1}{\omega} t^*, \quad r = R_0 r^*, \quad z = R_0 z^*, \quad \tau_{nn} = p_c \tau_{nn}^*, \quad (28)$$

where $\omega = 2\pi f$ and $p_c = \rho \omega^2 R_0^2$. It is assumed that the pulse is reflected entirely from the wall ($z = 0$) and subsequently interacts with the bubble a second time.

IV. COMPARISON OF BEM WITH THE SPHERICAL MODEL

The numerical results presented in this section use the following values of the shell thickness and surface tension parameters for the encapsulated microbubble, unless otherwise stated,

$$\varepsilon = 1\text{nm}, \quad \sigma = 0.051\text{N/m}. \quad (29)$$

These values are taken from Wu, Pepe, and Dewitt (2003) and were obtained using a mean square errors best fit for experimentally obtained values for the contrast agent MP1950. This is an experimental thin lipid-shelled ultrasound contrast agent with a decafluorobutane gas core. It has a monolayer lipid microbubble shell with a thickness of the order of a few nanometers.

In Figs. 2 and 3 the BEM model is compared to the solution of the spherical model (1) for an encapsulated microbubble forced by a Gaussian pulse with parameters:

$p_A = 200\text{kPa}$, $f = 1\text{MHz}$, $Re = 6.3$, $De = 0$ and $R_0 = 1\mu\text{m}$ in the absence of a rigid wall. The pressure of the pulse for the BEM code is measured at the node furthest from the wall and the ‘equivalent bubble radius’ is defined by

$$R_{eq} = \left(\frac{3V(t)}{4\pi} \right)^{1/3}$$

where $V(t)$ is the volume of the bubble at time t .

The models predict similar behaviour initially. However, the pressure begins to deviate significantly as the BEM bubble translates downwards due to the imparted energy from the pulse. The possibility for bubble translation does not exist within the spherical model. Also, as can be seen in Fig. 4, the EMB is shown to flatten considerably as it moves downwards (light blue) and, as it shrinks, the surface becomes very distorted until the simulation terminates when two nodes become too close to one another (yellow). The BEM model thus predicts that an encapsulated microbubble can deform significantly, and potentially disintegrate, even at these relatively modest pressure amplitudes. This agrees with experimental observations which suggest that contrast microbubbles can sometimes be destroyed during routine examinations (Averkiou *et al.* (2003)).

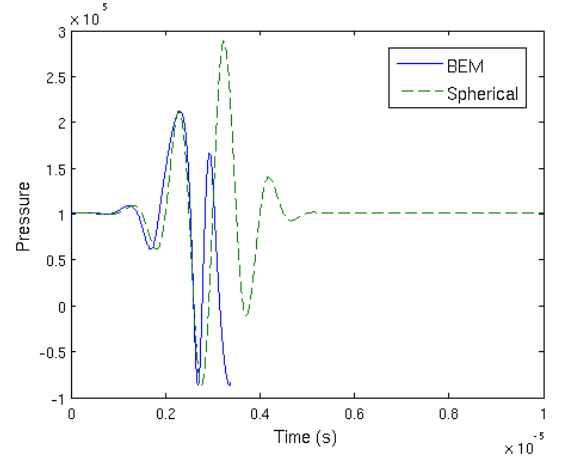


FIG. 2. Evolution of the pressure at node 1 of an EMB forced by a Gaussian pulse with $p_A = 200\text{kPa}$, $f = 1\text{MHz}$, $Re = 6.3$, $De = 0$ and $R_0 = 1\mu\text{m}$.

Figs. 5 and 6 show the evolution of the equivalent bubble radius and centroid, respectively, for $p_A = 100\text{kPa}$, $f = 2\text{MHz}$, $Re = 6.3$ and $R_0 = 1\mu\text{m}$. Similar to the previous case, the models agree initially with similar dynamics in terms of bubble radius up to roughly $3\mu\text{s}$. At this point the translation of the bubble in the direction of the pulse and the accompanying change in bubble shape from spherical to non-spherical in the BEM simulations lead to some differences in predictions. Note, however, that the deviation in radius from $R_0 = 1$ is of the same order for both simulations (see Fig. 5); both predict non-linear, stable oscillations before a return to the initial ra-

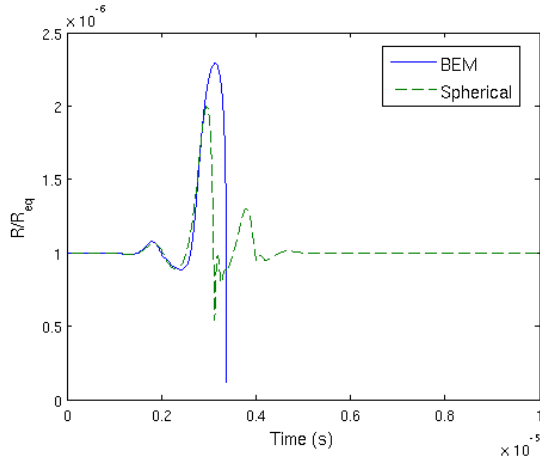


FIG. 3. Evolution of the equivalent bubble radius of an EMB forced by a Gaussian pulse with $p_A = 200\text{kPa}$, $f = 1\text{MHz}$, $Re = 6.3$ and $R_0 = 1\mu\text{m}$.

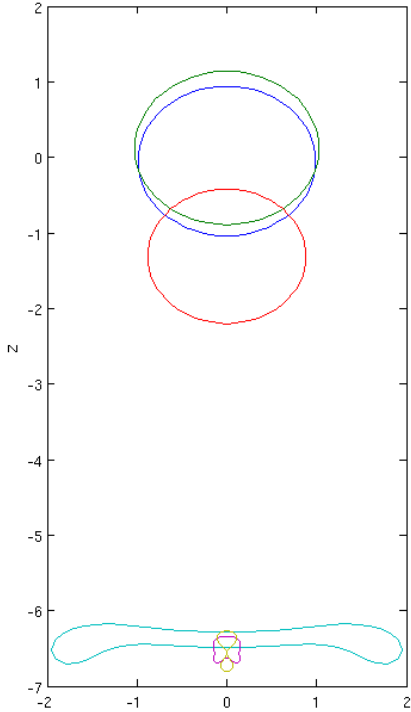


FIG. 4. Bubble surfaces for $p_A = 200\text{kPa}$, $f = 1\text{MHz}$, $Re = 6.3$ and $R_0 = 1\mu\text{m}$. The times are $t = 0.000\text{s}$ (dark blue), $t = 0.1503 \times 10^{-5}\text{s}$ (green), $t = 0.2104 \times 10^{-5}\text{s}$ (red), $t = 0.3016 \times 10^{-5}\text{s}$ (light blue), $t = 0.3321 \times 10^{-5}\text{s}$ (pink) and $t = 0.3376 \times 10^{-5}\text{s}$ (yellow).

dius for these parameters. Clearly, the spherical model is unable to describe realistic dynamics of EMBs. Although the predictions are qualitatively similar to those obtained using the axisymmetric BEM model for some parameters, the translational movement of the bubble and the subsequent non-spherical oscillations can lead to significantly different results when compared with the

spherical model.

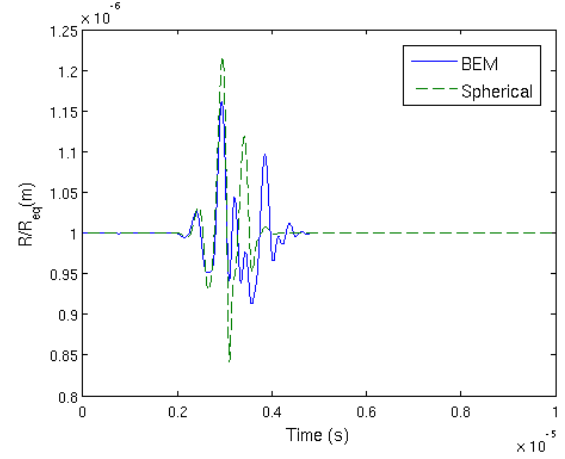


FIG. 5. Evolution of the equivalent bubble radius of an EMB forced by a Gaussian pulse with $p_A = 100\text{kPa}$, $f = 2\text{MHz}$, $Re = 6.3$ and $R_0 = 1\mu\text{m}$.

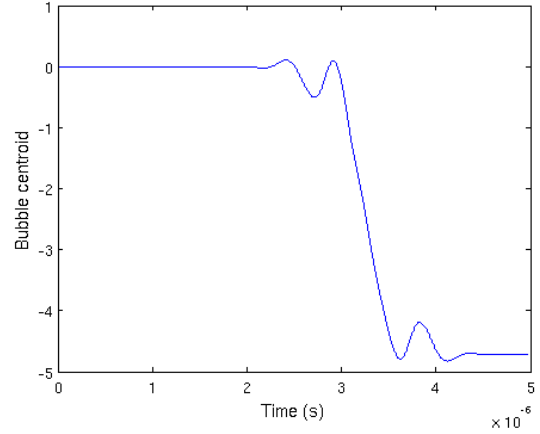


FIG. 6. Evolution of the centroid of an EMB forced by a Gaussian pulse with $p_A = 100\text{kPa}$, $f = 2\text{MHz}$, $Re = 6.3$ and $R_0 = 1\mu\text{m}$.

V. MODEL PREDICTIONS

All the results presented in this section are concerned with the prediction of the dynamics of a bubble located near a rigid wall of infinite width along $z = 0$. Snapshots of a bubble surface in time are shown as a two-dimensional cut through the bubble, due to the assumed axisymmetry. The jet velocities shown in the figures are the velocities of the node on the bubble surface that is initially located furthest away from the wall. The wall pressures are calculated at the point $(r, z) = (0, 0)$.

1. Effect of Shell Thickness

The effect of shell width on the dynamics of an EMB is investigated for the particular case when the stand-off distance is $h = 5$. The characteristics of the pulse are $p_A = 2\text{MPa}$ and $f = 2\text{MHz}$. For a thin shell with $\varepsilon = 1\text{nm}$, the bubble begins to oscillate due to the pressure field until, at $t \approx 8$, significant movement towards the boundary is observed (Fig. 7). Increasing the shell thickness to $\varepsilon = 10\text{nm}$, smaller oscillations and less translational movement is seen initially due to the increased resistance of the shell to deformation. At $t \approx 14$, however, large growth is seen (??) due to the bubble entering a low pressure region of the applied pressure field. The bubble is ‘pushed’ by this forcing pressure towards the rigid wall and, due to this, remains in this low pressure region and continues to grow. Eventually the bubble moves very close to the wall and instabilities occur, particular in the jet velocities and wall pressures shown in Figs. 9 and 10.

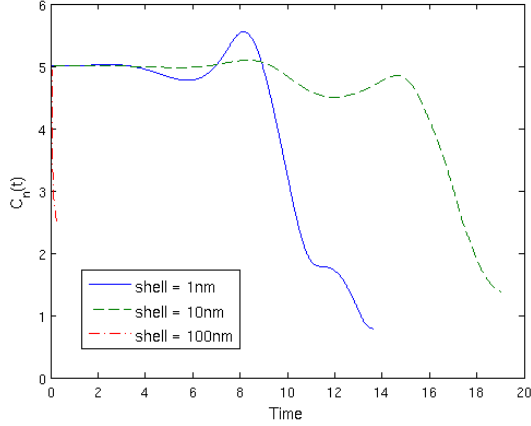


FIG. 7. Evolution of the bubble centroid for $h = 5$, $p_A = 2\text{MPa}$, $f = 2\text{MHz}$ and $\varepsilon = 1, 10, 100\text{nm}$

For both $\varepsilon = 1\text{nm}$ and $\varepsilon = 10\text{nm}$, the simulations are terminated when the bubble surface moves to be in close proximity to the rigid wall. At this point a very thin layer of fluid is trapped between the bubble and the wall, resulting in numerical instabilities. These instabilities are primarily responsible for the very large pressures that are generated at the wall as can be seen in Fig. 10 at $t \approx 13$ for $\varepsilon = 1\text{nm}$ and $t \approx 17$ for $\varepsilon = 10\text{nm}$. One technique that has been used to overcome these numerical difficulties is to numerically attach the bubble to the wall as described in Ni, Zhang, and Wu (2015). The adoption of this technique into the present model, however, is left for the future. Snapshots in time of the bubble surface are shown in Fig. 11 for the case $\varepsilon = 100\text{nm}$. The bubble undergoes severe deformation and rapidly moves towards the boundary on a much shorter time scale than the other cases (7) expanding as it does so. It grows to an equivalent bubble radius three times its initial radius over a

very short period of time (7). It is likely that this value of ε is at the limit for which the thin-shell assumption made in Eqn. (13) is valid.

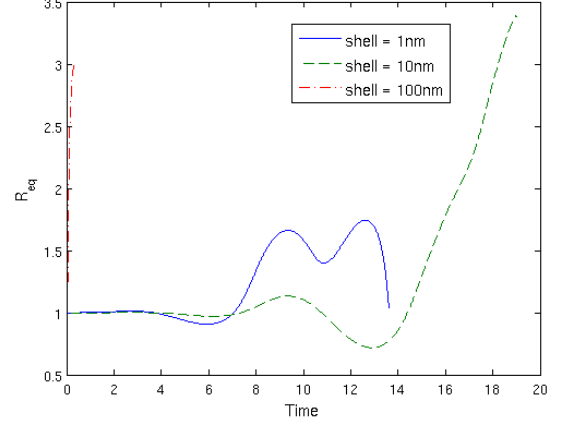


FIG. 8. Evolution of the equivalent bubble radius for $h = 5$, $p_A = 2\text{MPa}$, $f = 2\text{MHz}$ and $\varepsilon = 1, 10, 100\text{nm}$

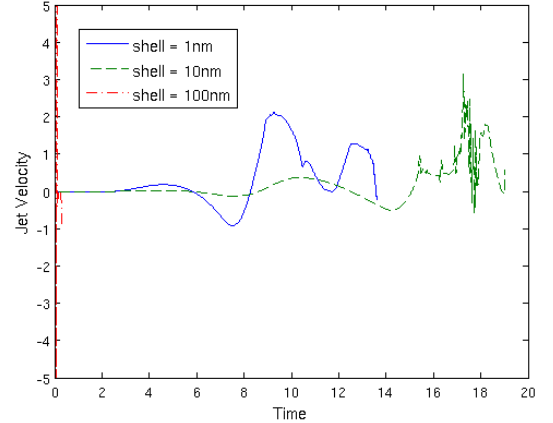


FIG. 9. Evolution of the jet velocity for $h = 5$, $p_A = 2\text{MPa}$, $f = 2\text{MHz}$ and $\varepsilon = 1, 10, 100\text{nm}$

2. Effect of Fluid Viscoelasticity

The viscoelasticity of the fluid is modelled using the Oldroyd-B equation. The constitutive equation (18) is an evolution equation for the polymer contribution to the stress. This is solved simultaneously with Eqns. (13,14) to update the system in time. Using the non-dimensionalisation given by Eqn. (28), the relative importance of fluid viscosity and elasticity can be investigated using the Reynolds (Re) and Deborah (De) numbers defined, respectively, by

$$Re = \frac{\rho w R_0^2}{\eta}, \quad De = \lambda w. \quad (30)$$

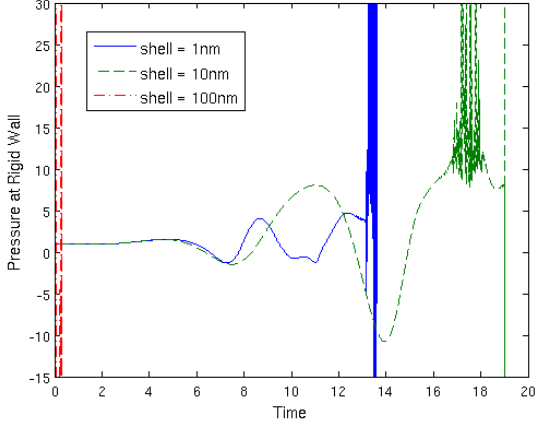


FIG. 10. Evolution of the pressure at the rigid wall for $h = 5$, $p_A = 2\text{MPa}$, $f = 2\text{MHz}$ and $\varepsilon = 1, 10, 100\text{nm}$

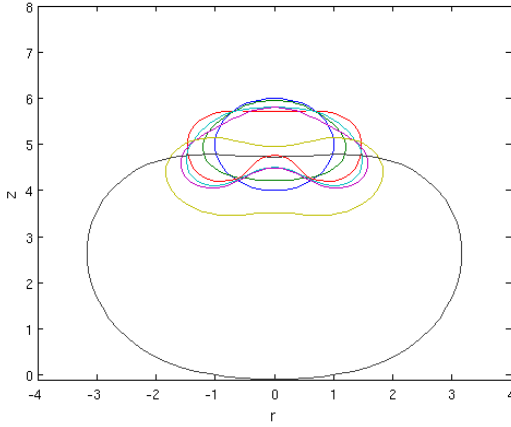


FIG. 11. Snapshots of the bubble surface for $\varepsilon = 100\text{nm}$, $h = 5$, $p_A = 2\text{MPa}$ and $f = 2\text{MHz}$. The plots run from top to bottom in time.

In Figs. 12 - 15 and Figs. 20 - 23, the effects of changing fluid viscosity are shown for small ($De = 0.5$) and large ($De = 10$) Deborah numbers, respectively. Walters and Phillips (2016) studied the effects of viscoelasticity on a clean, unforced cavitation bubble.

For $De = 0.5$, as the Reynolds number is increased (corresponding to a lower viscosity) a larger response to the acoustic forcing is observed. This is evidenced by the rapid translational movement of the bubble towards the boundary (Fig. 12), greater (initial) bubble growth (Fig. 13) and larger jet velocities (Fig. 14). For both $Re = 4$ and $Re = 10$, the bubbles grow rapidly and are pushed towards the boundary by the pressure field at a fairly uniform speed. Bubble collapse does not occur within the duration of the computations in these cases due to the onset of numerical instabilities. These occur when the bubble moves so close to the rigid wall that there is only a very thin layer of fluid between. When this occurs the computations are terminated before a liquid

jet (and transition to toroidal form) forms when $Re = 4$ and $Re = 10$.

For the more viscous case $Re = 1$ the growth of the bubble due to the pressure pulse is smaller. A violent collapse phase occurs at $t \approx 14$ (see Fig. 13) before the bubble swiftly rebounds to a volume more than 15 times its initial volume. The higher pressures attained for the case $Re = 1$ (see Fig. 15) are due to the smaller bubble volume and the resulting compression of the internal bubble contents. A liquid jet forms during the collapse, eventually impacting the far side and the bubble transitions to a toroidal form. Snapshots of the bubble surface are shown in each phase in Figs. 16 - 19. The initial, singly-connected stage is shown in Fig. 16 with the bubble moving towards the wall and adopting a pear-like shape prior to the formation of the liquid jet. The first toroidal phase is then shown in Fig. 17; initially the eye of the torus widens and the bubble moves slightly away from the wall. The bubble then re-expands and starts to move towards the wall once again. Due to the re-expansion, the eye of the torus begins to shrink (as seen by the diminishing distance between the torus and the vertical axis). Once the minimum distance of the bubble from the axis falls below a critical threshold (chosen to be 0.05 units), a numerical reconnection is employed. This process is essentially the reverse of the transition to the toroidal form and more details can be found in Walters (2015). A second liquid jet then forms (shown in Fig. 18) followed by a second toroidal phase shown in Fig. 19.

For the same range of Reynolds numbers, the bubble dynamics are shown in Figs. 20 - 22 for the (higher-elasticity) case $De = 10$. The effect of fluid viscosity is relatively insignificant in this case compared to the previous case ($De = 0.5$) since the elevated levels of fluid elasticity effectively negate most of the viscous effects. For the more viscous case $Re = 1$ the bubble actually grows slightly larger in size than for $Re = 4$ and $Re = 10$, although the jet velocities are slightly smaller (Figs. 21 and 22). This occurs because there is less translational movement than for the more viscous case, resulting in the bubble remaining in a lower pressure region of the pulse for longer. In all these cases the bubble becomes very distorted and the simulation terminates when two portions of the bubble surface become too close together, leading to instabilities. It is thought that at this point the bubble may fragment, although this phenomenon is not modelled here.

3. Effect of Pulse Frequency

For a spherical EMB, the effects of pulse frequency were investigated theoretically and experimentally by Wu, Pepe, and Dewitt (2003). The authors observed that lower-frequency ultrasound induced more vigorous oscillations under similar acoustic pressures. The effects of changing the pulse frequency on a non-spherical EMB are shown in Figs. 24 - 27 for a bubble in an Oldroyd-

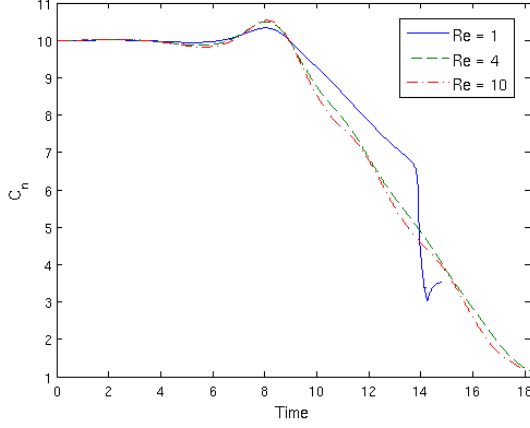


FIG. 12. Evolution of the bubble centroid position for parameters $h = 10$, $p_A = 2\text{MPa}$, $f = 2\text{MHz}$, $De = 0.5$ and $Re = 1, 4, 10$.

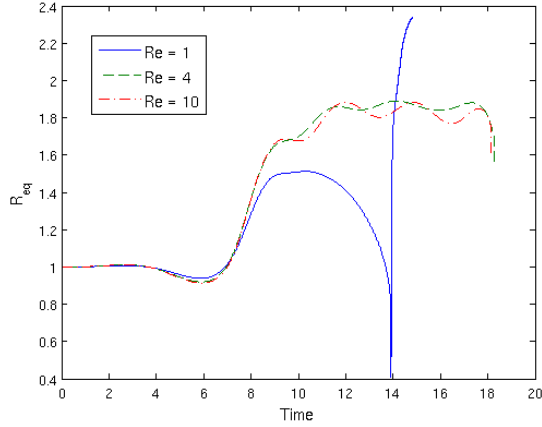


FIG. 13. Evolution of the equivalent bubble radius for parameters $h = 10$, $p_A = 2\text{MPa}$, $f = 2\text{MHz}$, $De = 0.5$ and $Re = 1, 4, 10$.

B fluid with $Re = 1$, $De = 0.5$. As for the spherical case, the initial response to the pulse is larger for a pulse frequency of $f = 1\text{MHz}$ than for the higher frequencies $f = 2\text{MHz}$ and $f = 4\text{MHz}$. This can be seen by noting the more rapid increase in bubble volume as well as the larger bubble volume attained (Fig. 24), and the earlier and larger initial translational movement (Fig. 25) at $t \approx 8$ as well as the greater jet velocities (Fig. 26) and pressures (Fig. 27) produced. When $f = 1\text{MHz}$, the bubble is then pushed by the pulse towards the rigid wall while remaining at roughly the same size (see Figs. 24 and 25). The simulation is terminated when the bubble becomes too close to the wall.

When $f = 2\text{MHz}$ the oscillating pressure pulse causes the bubble to collapse after its initial growth at $t \approx 14$, resulting in the formation of a liquid jet and subsequent transition to a toroidal form. Snapshots of the bubble

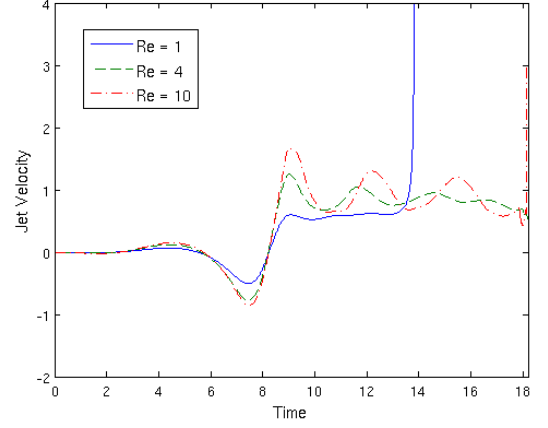


FIG. 14. Evolution of the jet velocity for parameters $h = 10$, $p_A = 2\text{MPa}$, $f = 2\text{MHz}$, $De = 0.5$ and $Re = 1, 4, 10$.

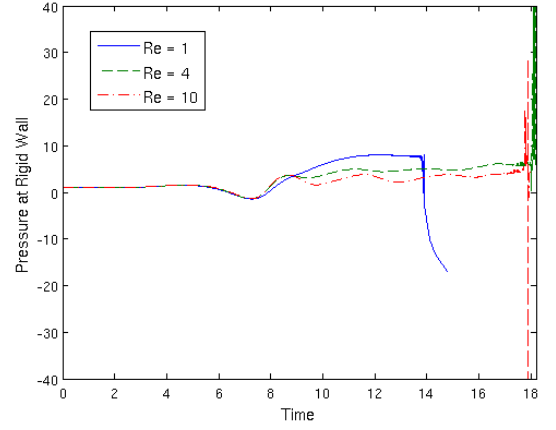


FIG. 15. Evolution of the pressure at the rigid wall for parameters $h = 10$, $p_A = 2\text{MPa}$, $f = 2\text{MHz}$, $De = 0.5$ and $Re = 1, 4, 10$.

surface for this case are shown in Figs. 16 - 19. When $f = 4\text{MHz}$ the bubble oscillates until $t \approx 15$ before undergoing rapid growth as it moves towards the bubble. The computations are terminated at $t \approx 25$ when the bubble is close to the wall.

4. Effect of Pulse Strength

So far in this paper, numerical predictions of bubble dynamics have been presented for a pressure amplitude of $P_A = 2\text{MPa}$ since this is a typical value for pulse strength used in sonoporation. In ultrasound contrast imaging, however, the pressure amplitudes are typically of the order of 100kPa. In Figs. 28 - 31, results are presented for a fixed pulse frequency and a range of pressure amplitudes: $P_A = 400\text{kPa}, 800\text{kPa}, 2\text{MPa}$.

The majority of EMBs have been shown (von Bibra

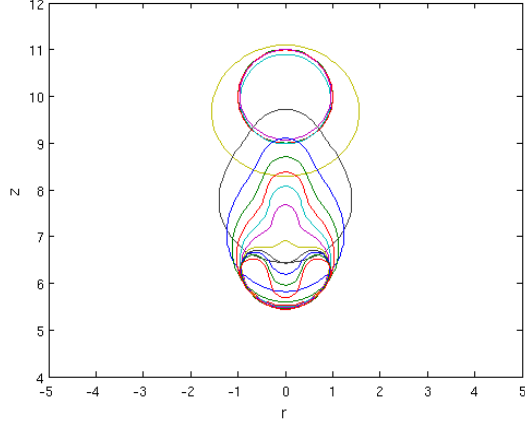


FIG. 16. Snapshots of the bubble surface in the first singly-connected phase for $Re = 1$, $De = 0.5$, $\varepsilon = 1\text{nm}$, $h = 10$, $p_A = 2\text{MPa}$ and $f = 2\text{MHz}$.

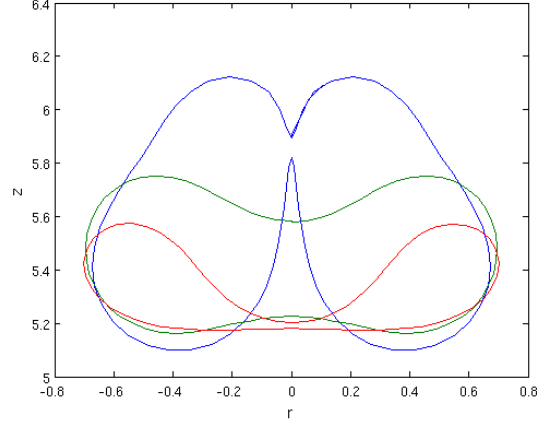


FIG. 18. Snapshots of the bubble surface in the second singly-connected phase for $Re = 1$, $De = 0.5$, $\varepsilon = 1\text{nm}$, $h = 10$, $p_A = 2\text{MPa}$ and $f = 2\text{MHz}$.

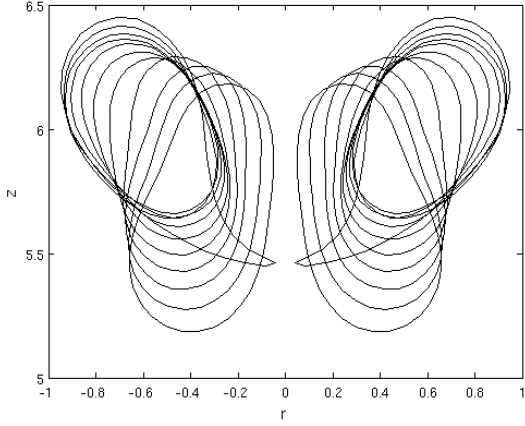


FIG. 17. Snapshots of the bubble surface in the first toroidal phase for $Re = 1$, $De = 0.5$, $\varepsilon = 1\text{nm}$, $h = 10$, $p_A = 2\text{MPa}$ and $f = 2\text{MHz}$.

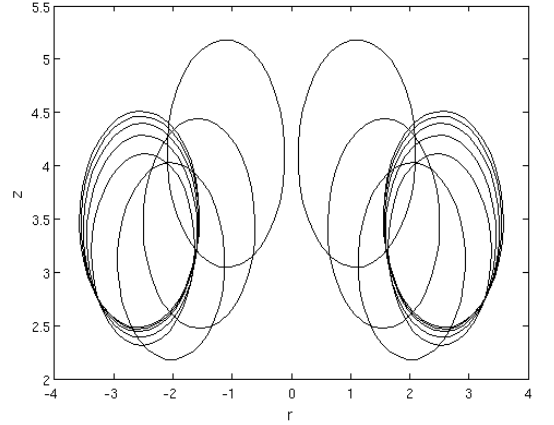


FIG. 19. Snapshots of the bubble surface in the second toroidal phase for $Re = 1$, $De = 0.5$, $\varepsilon = 1\text{nm}$, $h = 10$, $p_A = 2\text{MPa}$ and $f = 2\text{MHz}$.

et al. (1999)) to undergo stable, harmonic oscillations for pressure amplitudes in the range 50kPa - 200kPa, with higher amplitudes potentially leading to spontaneous acoustic emissions and bubble fragmentation. The numerical predictions presented here agree well with these experimental findings since in the lowest amplitude case considered for which $p_A = 400\text{kPa}$, the bubble undergoes stable oscillations before reaching a steady configuration that corresponds approximately to its initial volume and position. In the case for which $p_A = 800\text{kPa}$, the bubble grows rapidly to a large size as it is pushed towards the boundary. The computations are terminated when the bubble becomes too close to the wall. For $p_A = 2\text{MPa}$ after a steady initial period until $t \approx 10$ the bubble moves rapidly towards the wall increasing in volume as it does so.

VI. CONCLUSIONS

In this paper an encapsulated microbubble in a viscoelastic fluid forced by a pressure field is modelled using a modified boundary element method. Viscous and interfacial terms are included to account for the influence of the shell using an extension of the spherical model developed by Morgan *et al.* (2000).

For a bubble in an infinite fluid, the non-spherical BEM simulations produce significantly different results to the spherical model. This is due to the translational movement of the bubble in the direction of the pressure field and non-spherical deviations. These mechanisms (which are not able to be predicted by the spherical model) are found to potentially cause disintegration of an EMB, even at relatively low pressure amplitudes.

In agreement with Wang, Manmi, and Calvisi (2015),

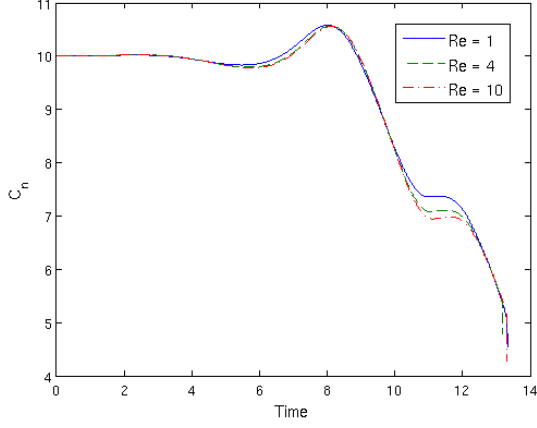


FIG. 20. Evolution of the bubble centroid position for parameters $h = 10$, $p_A = 2\text{MPa}$, $f = 2\text{MHz}$, $De = 10$ and $Re = 1, 4, 10$.

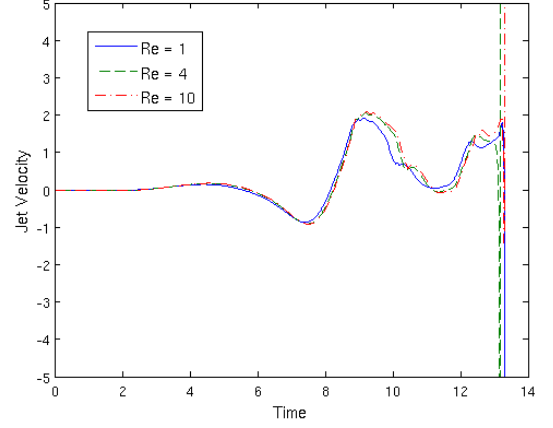


FIG. 22. Evolution of the jet velocity for parameters $h = 10$, $p_A = 2\text{MPa}$, $f = 2\text{MHz}$, $De = 10$ and $Re = 1, 4, 10$.

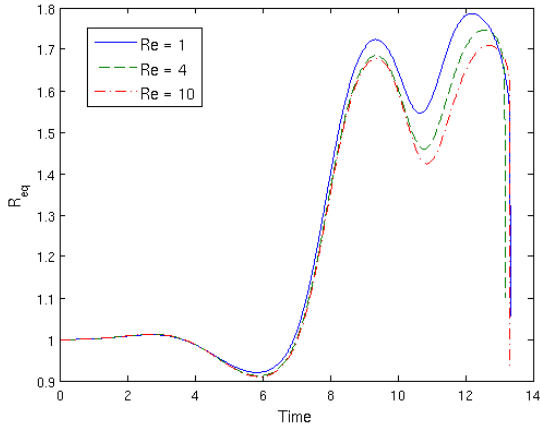


FIG. 21. Evolution of the equivalent bubble radius for parameters $h = 10$, $p_A = 2\text{MPa}$, $f = 2\text{MHz}$, $De = 10$ and $Re = 1, 4, 10$.

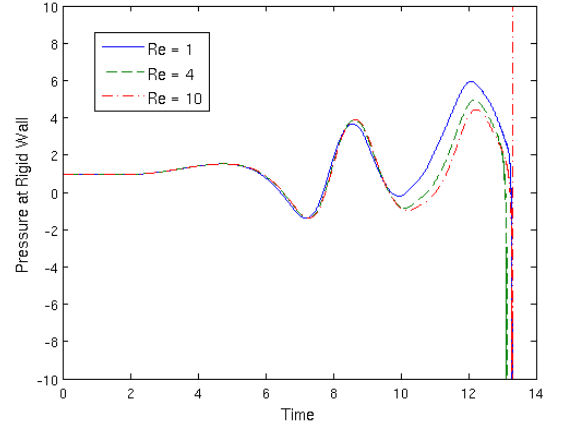


FIG. 23. Evolution of the pressure at the rigid wall for parameters $h = 10$, $p_A = 2\text{MPa}$, $f = 2\text{MHz}$, $De = 10$ and $Re = 1, 4, 10$.

we have shown that increasing the shell thickness reduces the translational movement and jet velocities of the EMB. This is expected since a thicker shell provides more stability making the bubble more resistant to deformation. For $\varepsilon = 100\text{nm}$, however, unphysical behaviour is observed. This is most likely due to the value of ε being close to the limit of validity of the thin shell assumption, leading to numerical errors.

The effect of changing fluid viscoelasticity is also investigated by altering the Reynolds and Deborah numbers. The effects are similar to those seen for a clean cavitation bubble; more details of which can be found in Walters and Phillips (2016). In general, an increase in fluid viscosity results in reduced bubble wall velocities. However, due to the acoustic forcing, this is not always the case. Since fluid viscosity also has an effect on the translational movement of the bubble, it is possible that an increase in viscosity causes the bubble to persist in a high pressure

region for longer and experience a more violent collapse. Changes in viscosity is also found to have less of an effect for more elastic fluids, since elasticity essentially negates the effect of fluid viscosity.

Finally, the effects of the properties of the acoustic pulse, viz. pulse frequency (f) and strength (p_A), on bubble dynamics have also been considered. A larger response is initially seen for lower frequencies, although further studies are required particularly when the bubble moves to be in close proximity to the wall. In this case the numerical method will need to be modified to model the attachment of the bubble to the wall so that the simulations can be continued to obtain an improved understanding of the effect of frequency for an EMB near a rigid wall. A higher pulse strength naturally leads to higher jet velocities and more distortion of the bubble although it is found that the EMB can become very distorted, and can potentially disintegrate, even at the rel-

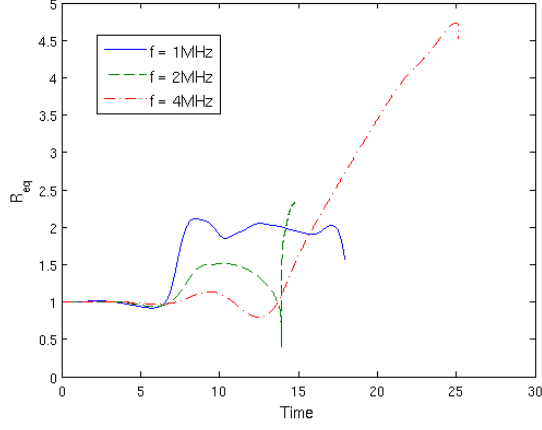


FIG. 24. Equivalent bubble radius vs. time for $Re = 1$, $De = 0.5$, $\varepsilon = 1\text{nm}$, $h = 5$, $P_A = 2\text{MPa}$ and $f = 1, 2, 4\text{MHz}$.

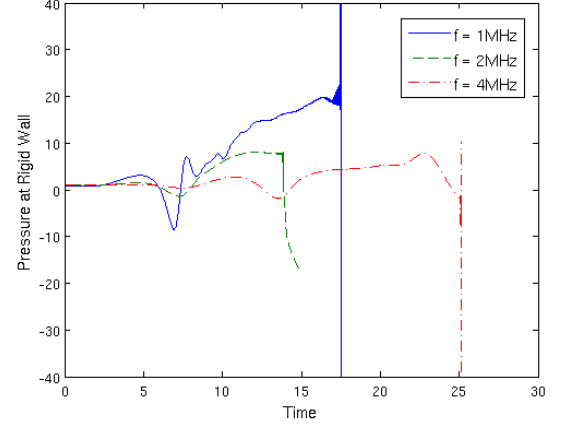


FIG. 27. Pressure at the rigid wall for $Re = 1$, $De = 0.5$, $\varepsilon = 1\text{nm}$, $h = 5$, $P_A = 2\text{MPa}$ and $f = 1, 2, 4\text{MHz}$.

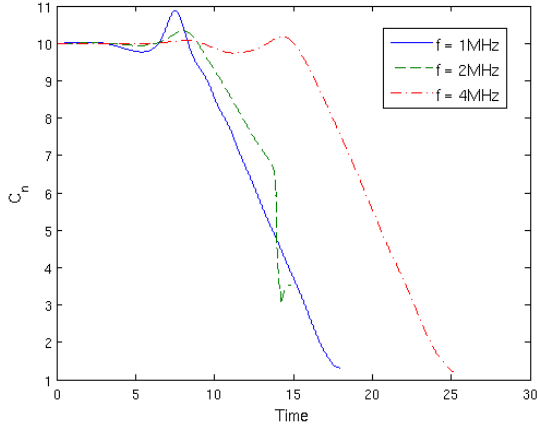


FIG. 25. Bubble centroid position vs. time for $Re = 1$, $De = 0.5$, $\varepsilon = 1\text{nm}$, $h = 5$, $P_A = 2\text{MPa}$ and $f = 1, 2, 4\text{MHz}$.

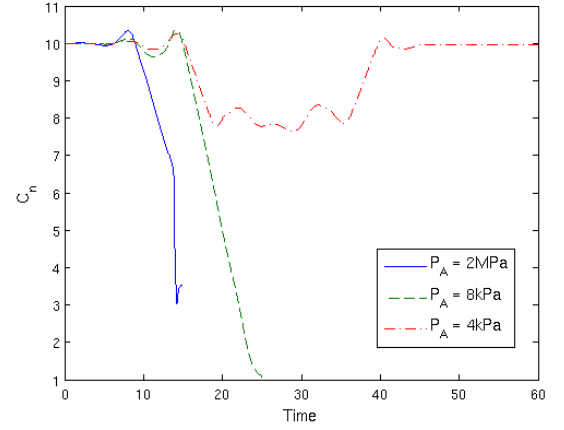


FIG. 28. Bubble centroid position for $Re = 1$, $De = 0.5$, $\varepsilon = 1\text{nm}$, $h = 10$, $f = 2\text{MHz}$ and $P_A = 400\text{kPa}, 800\text{kPa}, 2\text{MPa}$.

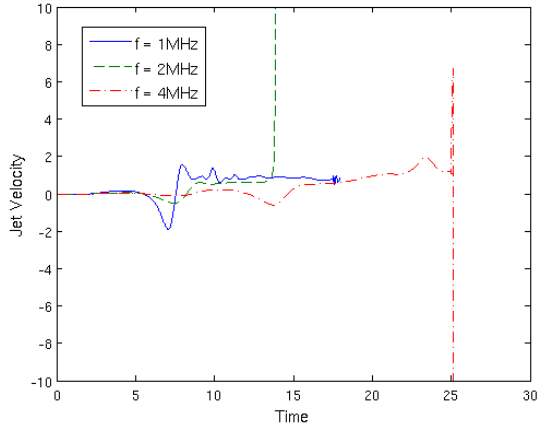


FIG. 26. Jet velocities for $Re = 1$, $De = 0.5$, $\varepsilon = 1\text{nm}$, $h = 5$, $P_A = 2\text{MPa}$ and $f = 1, 2, 4\text{MHz}$.

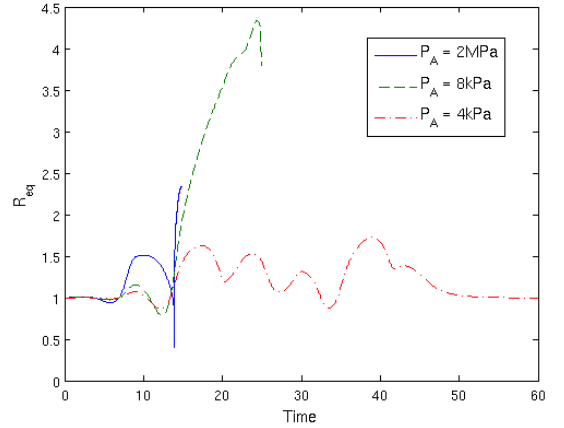


FIG. 29. Equivalent bubble radius for $Re = 1$, $De = 0.5$, $\varepsilon = 1\text{nm}$, $h = 10$, $f = 2\text{MHz}$ and $P_A = 400\text{kPa}, 800\text{kPa}, 2\text{MPa}$.

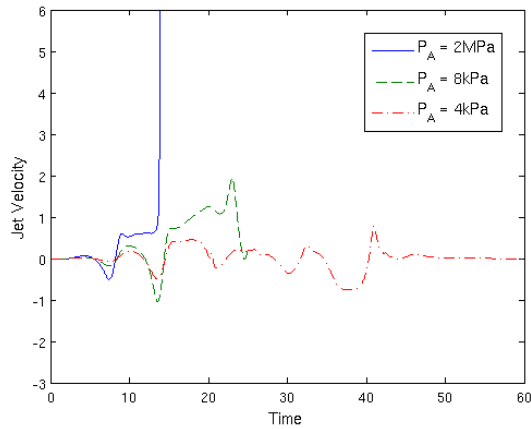


FIG. 30. Jet velocities for $Re = 1$, $De = 0.5$, $\varepsilon = 1\text{nm}$, $h = 10$, $f = 2\text{MHz}$ and $P_A = 400\text{kPa}$, 800kPa , 2MPa .

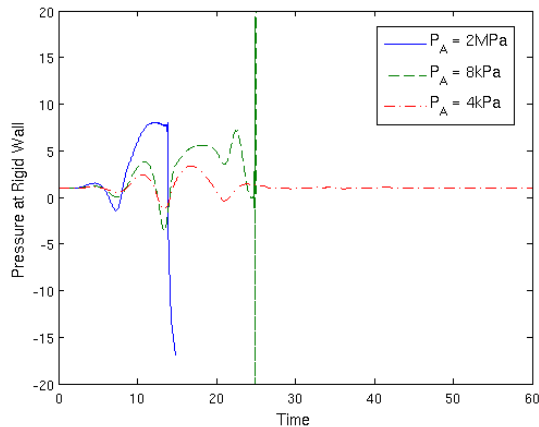


FIG. 31. Pressures at the rigid wall for $Re = 1$, $De = 0.5$, $\varepsilon = 1\text{nm}$, $h = 10$, $f = 2\text{MHz}$ and $P_A = 400\text{kPa}$, 800kPa , 2MPa .

atively low pressure amplitudes employed in routine ultrasound scans.

ACKNOWLEDGMENTS

This research was supported through a PhD studentship funded by Cardiff School of Mathematics. We would like to thank Dr. S.J. Lind for providing his BEM code which provided the basis for comparisons between the non-singular and standard BEM formulations.

REFERENCES

- Allen, J. and Roy, R., "Dynamics of gas bubbles in viscoelastic fluids. I. Linear viscoelasticity," *J. Acoust. Soc. Am.* **107**, 3167–3178 (2000a).
- Allen, J. and Roy, R., "Dynamics of gas bubbles in viscoelastic fluids. I. Nonlinear viscoelasticity," *J. Acoust. Soc. Am.* **108**, 1640–1650 (2000b).
- Averkiou, M., Powers, J., Skyba, D., Bruce, M., and Jensen, S., "Ultrasound contrast imaging research," *Ultrasound Quarterly* **19**, 27–37 (2003).
- Bao, S., Thrall, B. D., and Miller, D. L., "Transfection of a reporter plasmid into cultured cells by sonoporation in vitro," *Ultrasound Med. Biol.* **23**, 953–959 (1997).
- Batchelor, G. K., *An Introduction to Fluid Dynamics* (Cambridge University Press, London, 1967).
- von Bibra, H., Voigt, J., Fröman, M., Bone, D., Wranne, B., and Juhlin-Dannfeldt, A., "Interaction of microbubbles with ultrasound," *Echocardiography* **16**, 733–741 (1999).
- Brennen, C. E., *Cavitation and Bubble Dynamics* (Oxford University Press, Oxford, 1995).
- Brujan, E. A., "A first-order model for bubble dynamics in a compressible viscoelastic liquid," *J. Non-Newtonian Fluid Mech.* **84**, 83–103 (1999).
- Brujan, E. A., "The equation of bubble dynamics in a compressible linear viscoelastic liquid," *J. Fluid Dyn. Res.* **29**, 287–294 (2001).
- Brujan, E. A., "Cavitation bubble dynamics in non-Newtonian fluids," *Polym. Eng. Sci.* **49**, 419–431 (2009).
- Church, C. C., "The effects of an elastic solid surface layer on the radial pulsations of gas bubbles," *J. Acoust. Soc. Am.* **97**, 1510–1521 (1995).
- Cosgrove, D., "Ultrasound contrast agents: An overview," *Eur. J. Radiol.* **60**, 324–330 (2006).
- Doinikov, A. A., Zhao, S., and Dayton, P. A., "Modeling of the acoustic response from contrast agent microbubbles near a rigid wall," *Ultrasonics* **49**, 195–201 (2009).
- Fogler, H. and Goddard, J., "Collapse of spherical cavities in viscoelastic fluids," *Phys. Fluids* **13**, 1135–1141 (1970).
- Foteinopoulou, K. and Laso, M., "Numerical simulation of bubble dynamics in a Phan-Thien-Tanner liquid: Nonlinear shape and size oscillatory response under periodic pressure," *Ultrasonics* **50**, 758–776 (2010).
- Glazman, R. E., "Effects of adsorbed films on gas bubble radial oscillations," *J. Acoust. Soc. Am.* **74**, 980–986 (1983).
- Hoff, L., *Acoustic characterization of contrast agents for medical ultrasound imaging* (Springer Science & Business Media, 2001).
- Johnsen, E. and Colonius, T., "Shock-induced collapse of a gas bubble in shockwave lithotripsy," *J. Acoust. Soc. Am.* **124**, 2011–2020 (2008).
- Johnsen, E. and Colonius, T., "Numerical simulations of non-spherical bubble collapse," *J. Fluid Mech.* **629**, 231–262 (2009).
- Khismatullin, D. and Nadim, A., "Radial oscillations of encapsulated microbubbles in viscoelastic liquids," *Phys. Fluids* **14**, 3534–3557 (2002).
- Lind, S. J. and Phillips, T. N., "Spherical bubble collapse in viscoelastic fluids," *J. Non-Newtonian Fluid Mech.* **165**, 56–64 (2010).
- Lind, S. J. and Phillips, T. N., "The influence of viscoelasticity on the collapse of cavitation bubbles near a rigid boundary," *Theor. Comput. Fluid Dyn.* **26**, 245–277 (2012).
- Lind, S. J. and Phillips, T. N., "Bubble collapse in compressible fluids using a spectral element marker particle method. Part 2. Viscoelastic fluids," *Int. J. Numer. Methods Fluids* **71**, 1103–1130 (2013).
- Miller, D. L., Pislaru, S. V., and Greenleaf, J. F., "Sonoporation: Mechanical DNA delivery by ultrasonic cavitation," *Somat. Cell. Molec. Gen.* **27**, 115–134 (2002).
- Morgan, K. E., Allen, J. S., Dayton, P. A., Chomas, J. E., Klibanov, A. L., and Ferrara, K. E., "Experimental and theoretical evaluation of microbubble behaviour: effect of transmitted phase and bubble size," *IEEE Trans. Ultrason. Ferroelectr. Control* **47**, 1494–1509 (2000).
- Ni, B. Y., Zhang, A. M., and Wu, G. X., "Numerical and experimental study of bubble impact on a solid wall," *J. Fluid Eng.* **137**, 1–16 (2015).

- Rayleigh, L., “On the pressure developed in a liquid during the collapse of a spherical cavity,” *Phil. Mag.* **34**, 94–98 (1917).
- Sun, Q., Klaseboer, E., Khoo, B. C., and Chan, D. Y. C., “A robust and non-singular formulation of the boundary integral method for the potential problem,” *Eng. Anal. Bound. Elem.* **43**, 117–123 (2014).
- Taib, B. B., *Boundary integral method applied to cavitation bubble dynamics*, Ph.D. thesis, University of Wollongong (1985).
- Walters, M. J., *An Investigation into the Effects of Viscoelasticity on Cavitation Bubble Dynamics with Applications to Biomedicine*, Ph.D. thesis, Cardiff University (2015).
- Walters, M. J. and Phillips, T. N., “A non-singular boundary element method for modelling bubble dynamics in viscoelastic fluids,” *J. Non-Newtonian Fluid Mech.* **235**, 109–124 (2016).
- Wang, Q., Manmi, K., and Calvisi, M. L., “Numerical modeling of the 3D dynamics of ultrasound contrast agent microbubbles using the boundary integral method,” *Phys. Fluids* **27**, 022104 (2015).
- Wang, Q. X., Yeo, K. S., Khoo, B. C., and Lam, K. Y., “Vortex ring modelling of toroidal bubbles,” *Theor. Comput. Fluid Dyn.* **19**, 303–317 (2005).
- Wells, P. N. T., “Ultrasound imaging,” *Phys. Med. Biol.* **51**, R83–R89 (2006).
- Wu, J., Pepe, J., and Dewitt, W., “Nonlinear behaviours of contrast agents relevant to diagnostic and therapeutic applications,” *Ultrasound Med. Biol.* **29**, 555–562 (2003).
- Yang, X. and Church, C., “A model for the dynamics of gas bubbles in soft tissue,” *J. Acoust. Soc. Am.* **118**, 3595–3606 (2005).